Industrial Chemistry & Materials

ROYAL SOCIETY OF CHEMISTRY

PAPER

View Article Online
View Journal

Cite this: DOI: 10.1039/d5im00025d

Deactivation mechanisms of Cu–Zn–Al_2O_3 in CO_2 hydrogenation induced by SO_2 exposure†

Xuan Bie,[a] Ruoyu Wu,[a] Bocheng Yu,[a] Xuelong Quan,[a] Shiyu Zhang,[a] Qinghai Li,[ab] Yanguo Zhang[ab] and Hui Zhou *[ab]

The presence of sulfur compounds, particularly SO_2, is known to significantly degrade the performance of metal-based catalysts, posing a significant challenge in CO_2 hydrogenation reactions. In this study, we systematically investigate the impact of SO_2 on Cu–ZnO–Al_2O_3 catalysts for CO_2 hydrogenation to elucidate the deactivation mechanisms. Our findings reveal that SO_2 adsorption leads to the formation of surface sulfate and sulfite species, which effectively block active sites, impeding the adsorption and activation of reactants. Moreover, SO_2 exposure inhibits CO desorption, further compromising catalytic efficiency. In parallel, progressive sulfidation of Cu and ZnO results in the formation of catalytically inactive CuS, Cu_2S, and ZnS phases, ultimately leading to complete catalyst deactivation. These results highlight the dual role of sulfur species in both surface passivation *via* sulfates/sulfites deposition and irreversible structural transformation *via* sulfidation. Our study provides new insights into the SO_2-induced catalyst deactivation in CO_2 hydrogenation and offers a theoretical foundation for enhancing CO_2 hydrogenation reactions, with implications for optimizing environmentally sustainable catalytic systems in industrial applications.

Received 12th February 2025,
Accepted 27th May 2025

DOI: 10.1039/d5im00025d

rsc.li/icm

Keywords: CO_2 hydrogenation; The role of SO_2; Deactivation; Phase transition; RWGS.

1 Introduction

The increasing global concern over greenhouse gas emissions has led to significant interest in technologies aimed at reducing CO_2 concentrations in the atmosphere.[1–3] CO_2 hydrogenation has emerged as a promising pathway for the utilization of CO_2, enabling its conversion into valuable chemicals such as CO, methanol, and other hydrocarbons.[4–8] These processes not only offer a sustainable route to produce fuels and chemicals but also contribute to reducing the overall CO_2 footprint.[9,10] However, the practical implementation of CO_2 hydrogenation, particularly in industrial settings, faces several challenges due to the presence of impurities in feed gases, including sulfur-containing compounds such as sulfur dioxide (SO_2).[11–13]

SO_2 is a major contaminant commonly found in flue gases from coal-fired power plants, especially those utilizing pulverized coal combustion.[14,15] The flue gas typically contains a mixture of gases such as CO_2, nitrogen oxides (NO_x), and SO_2, which can have detrimental effects on catalytic processes.[14,16,17] In CO_2 hydrogenation, the presence of SO_2 is particularly concerning, as it is known to poison metal catalysts by binding to active sites and forming inactive sulfur compounds, leading to catalyst deactivation.[18–20] Understanding the impact of SO_2 on catalyst performance is critical for optimizing CO_2 hydrogenation processes, especially when considering the integration of these processes with industrial CO_2 capture systems, where SO_2 contamination is inevitable.

Previous studies have highlighted the negative impact of sulfur compounds on various catalytic systems, including those based on transition metals such as Cu, Ni, and Fe.[18,21–24] For the Cu-SSZ-13 catalyst, SO_2 poisoning under standard NH_3-SCR conditions resulted in mostly ammonium sulfate formation at 200 °C, whereas copper sulfates were predominant after poisoning at 400 °C under the conditions of 30 ppm SO_2, 8% O_2, 5% H_2O, 400 ppm NH_3 and 400 ppm NO.[25] In the integrated CO_2 capture and utilization (ICCU) process, exposure to SO_2 leads to the formation of thermally stable $CaSO_4$ product which, in turn, drastically reduces CO_2 capture capacity due to increased mass transfer resistance.[26] Despite these findings, while the negative impact of SO_2 on catalytic performance is well-established, comprehensive studies that investigate the specific mechanisms by which SO_2 affects catalytic activity in CO_2 hydrogenation remain limited.

This study aims to systematically investigate the influence of SO_2, derived from pulverized coal boiler flue gas, on the

[a] Key Laboratory for Thermal Science and Power Engineering of Ministry of Education, Beijing Key Laboratory of CO_2 Utilization and Reduction Technology, Department of Energy and Power Engineering, Tsinghua University, Beijing 100084, P.R. China. E-mail: huizhou@tsinghua.edu.cn
[b] Shanxi Research Institute for Clean Energy, Tsinghua University, Shanxi, Taiyuan 030000, P.R. China

† Electronic supplementary information (ESI) available: Fig. S1–S9, Tables S1–S3. See DOI: https://doi.org/10.1039/d5im00025d

performance of industrial catalyst Cu–ZnO–Al_2O_3 catalysts during CO_2 hydrogenation. By combining advanced characterization techniques such as X-ray photoelectron spectroscopy (XPS), scanning transmission electron microscopy (STEM), *operando* diffuse reflectance infrared Fourier transform spectroscopy (DRIFTS), and *operando* X-ray diffraction (XRD), we aim to elucidate the poisoning and deactivation mechanisms of SO_2 on the catalyst. The results reveal that exposure to SO_2 induces irreversible catalyst deactivation, with both Cu and Zn species fully converted into metal sulfides (Cu_2S, CuS, and ZnS). Additionally, sulfide and sulfate species accumulate on the catalyst surface. These findings offer valuable insights into the mechanisms driving catalyst deactivation, paving the way for strategies to enhance the long-term stability and performance of CO_2 hydrogenation processes under industrial conditions.

2 Results and discussion

2.1 Catalytic performance

The CO_2 hydrogenation was conducted in a quartz tube reactor. The Cu–ZnO–Al_2O_3 catalyst demonstrated high catalytic performance over a temperature range of 300–700 °C with a H_2/CO_2 ratio of 1 : 1 (Fig. 1a). However, the introduction of SO_2 into the reaction stream induced a significant decrease in catalytic activity. At 300 °C, CO_2 conversion decreased from 4.1% to 0.16%, while CO selectivity slightly increased from 91.1% to 94.0% upon addition of 0.1% SO_2 (Fig. 1a and b). As the SO_2 concentration increased to 0.5% and 2.0%, the catalyst underwent complete deactivation (Fig. 1c), suggesting that higher SO_2 concentrations accelerate catalyst deactivation.

Higher temperatures exacerbated the deactivation of the catalyst. At 400 °C, CO_2 conversion decreased from 15.3% to 10.7% with the introduction of 0.1% SO_2, while CO selectivity increased from 91.5% to 94.3%. Increasing the SO_2 concentration to 0.5% further decreased CO_2 conversion to 4.9%, whereas CO selectivity was enhanced to 98.7%. These results suggest that SO_2 exposure primarily affects the formation of CH_4, with a more pronounced impact on CO_2 conversion and a shift in product distribution towards higher CO selectivity.

The CO_2 hydrogenation catalyst underwent significant deactivation upon SO_2 exposure, indicating partial irreversibility (Fig. 1d). At 500 °C and 0.5% SO_2, the CO_2 conversion initially decreased from 21.2% to 12.6%, while CO selectivity increased slightly from 95.3% to 96.7%. Furthermore, CO_2 conversion continued to decrease rather than stabilize at 12.6%. After 90 min of testing, the CO_2 conversion remained at 9.95%, while CO selectivity was 97.1%. Upon removal of SO_2 from the reaction stream, CO_2 conversion partially recovered to 13.4%, while CO selectivity remained around 97.3%. These results suggest that the deactivation is not fully reversible, implying partial permanent deterioration of the catalyst.

The experiment was extended until complete catalyst deactivation occurred (Fig. 2). Under SO_2-free conditions,

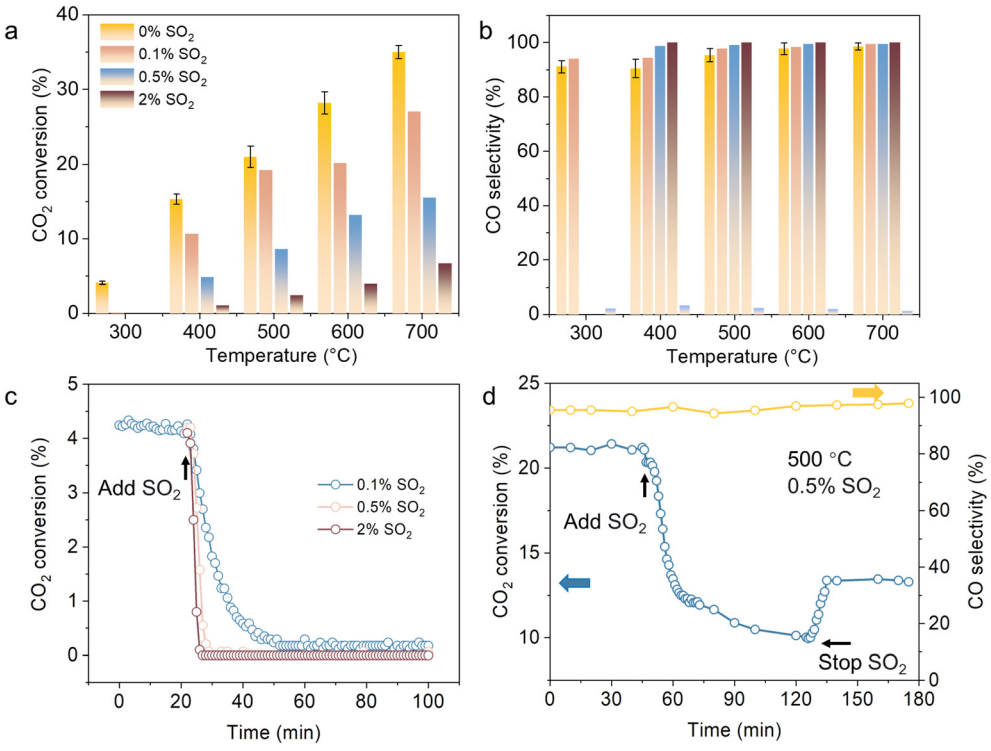

Fig. 1 Role of SO_2 on the catalyst performance. (a) CO_2 conversion and (b) CO selectivity over Cu–ZnO–Al_2O_3; (c) CO_2 conversion under different SO_2 concentrations over Cu–ZnO–Al_2O_3 at 300 °C; (d) changes in CO_2 conversion and CO selectivity when switching the gas composition (reaction conditions: 1 bar, H_2 : CO_2 : N_2 = 1 : 1 : 1, contact time: 0.05 s g mL^{-1}, WHSV: 72 000 cm^3 g^{-1} h^{-1}). Error bars were obtained from three repeated measurements.

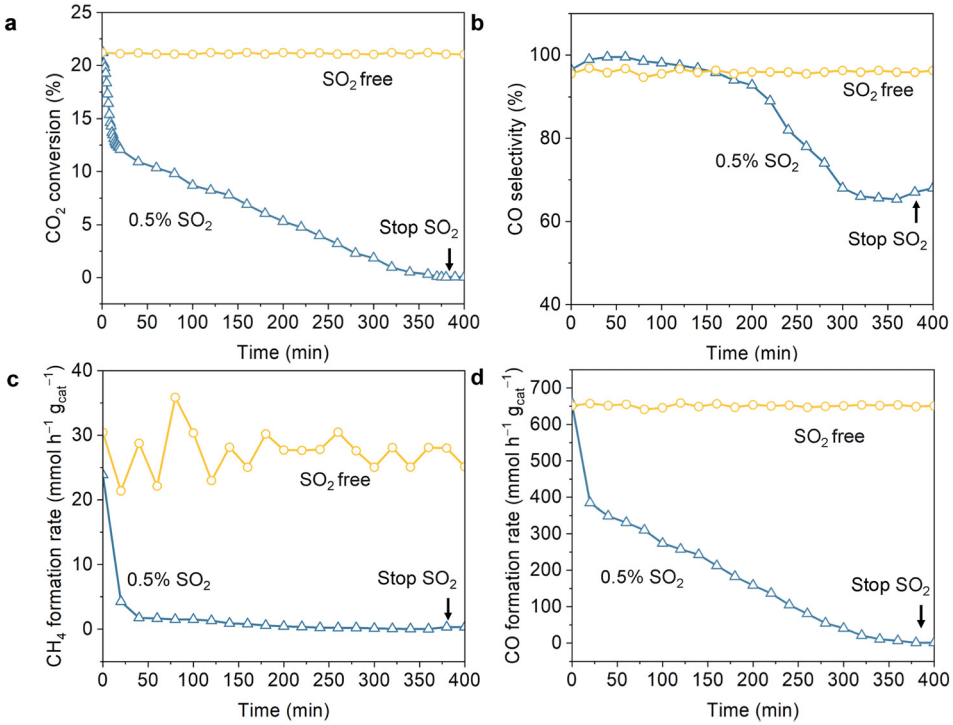

Fig. 2 SO_2-induced deactivation of the catalyst during CO_2 hydrogenation. Changes in (a) CO_2 conversion, (b) CO selectivity, (c) CH_4 formation rate, and (d) CO formation rate when switching the gas composition from H_2/CO_2 to H_2/CO_2 with 0.5% SO_2 (reaction conditions: 500 °C, 1 bar, $H_2:CO_2:N_2 = 1:1:1$, contact time: 0.05 s g mL^{-1}, WHSV: 72 000 cm^3 g^{-1} h^{-1}).

CO_2 conversion remained stable at 21.3% throughout the 400 min. In contrast, under 0.5% SO_2 conditions, CO_2 conversion steadily declined until full deactivation was observed (Fig. 2a). After the cessation of SO_2 flow, no recovery in CO_2 conversion was observed, indicating that deactivation was caused by irreversible poisoning. Regarding CO selectivity, it remained constant at 95.8% throughout the reaction under SO_2-free conditions (Fig. 2b). However, under 0.5% SO_2, CO selectivity initially increased slightly for the first 150 min, reaching a maximum of 99.5%. This increase was attributed to the rapid deactivation of CH_4 formation. Once SO_2 was introduced, the CH_4 formation rate decreased to 1.7 mmol h^{-1} g_{cat}^{-1} and dropped below 1 mmol h^{-1} g_{cat}^{-1} after 150 min (Fig. 2c). Subsequently, CO selectivity sharply declined to 65.3% due to the significant reduction in CO formation rate. The CO formation rate decreased from 657.8 to 212.8 mmol h^{-1} g_{cat}^{-1} after 150 min, and the continuous decline in CO formation contributed to the decline of the CO selectivity (Fig. 2d).

2.2 Deactivation mechanisms caused by SO_2

2.2.1 Effect of SO_2 on the surface chemical state of the catalyst. To investigate the deactivation mechanism, XPS was employed to analyze the surface changes of the fresh catalyst and the used catalysts after 400 min exposure to SO_2-free and 0.5% SO_2 conditions (Fig. 3 and S1–S3†). The Cu 2p spectra exhibited two peaks at binding energies of 932.7 eV and 952.6 eV, confirming that copper was present in the Cu^0/Cu^+ states in the fresh catalyst (Fig. S1†).[27] Similar spectra were observed for the catalysts used under both SO_2-free and 0.5% SO_2 conditions, indicating that copper remained in the Cu^0/Cu^+ states in all cases. No Cu^{2+} state was detected in either the fresh or used catalysts, indicating that copper did not undergo oxidation to Cu^{2+}.

Cu LMM Auger spectra were further analyzed to distinguish between Cu^0 and Cu^+ species (Fig. 3a). For the fresh catalyst, the Cu LMM spectra exhibited only Cu^0 (568.3 eV) species, with no evidence of Cu^+ (570.3 eV).[28] For the used catalysts under SO_2-free conditions and under 0.5% SO_2 conditions, both Cu^0 (568.3 eV) and Cu^+ (570.3 eV) species were present. We calculated the $Cu^+/(Cu^0 + Cu^+)$ ratio and found that for the used catalyst under SO_2-free conditions, Cu^+ constituted 18% of the surface copper (Table S1†). In contrast, for the used catalyst under 0.5% SO_2 conditions, Cu^+ constituted 58% of the surface copper. This indicates that SO_2 promoted the oxidation of metallic copper to Cu^+ state.

The Zn 2p spectra exhibited two peaks at binding energies of 1045.3 eV and 1022.2 eV, indicating that zinc predominantly exists in the Zn^{2+} state (Fig. S2†).[29] Further analysis of the Zn LMM spectra also revealed the presence of both Zn^{2+} and $Zn^{\delta+}$ species (Fig. 3b). All catalysts showed two peaks at 499.5 eV and 496.0 eV, indicating the presence of Zn^{2+} and $Zn^{\delta+}$ species on the catalysts, respectively.[30] The ratios of $Zn^{\delta+}/(Zn^{\delta+} + Zn^{2+})$ were calculated to be 37%, 37%, and 33% for the fresh catalyst, and for the used catalysts under SO_2-free and 0.5% SO_2 conditions, respectively (Table

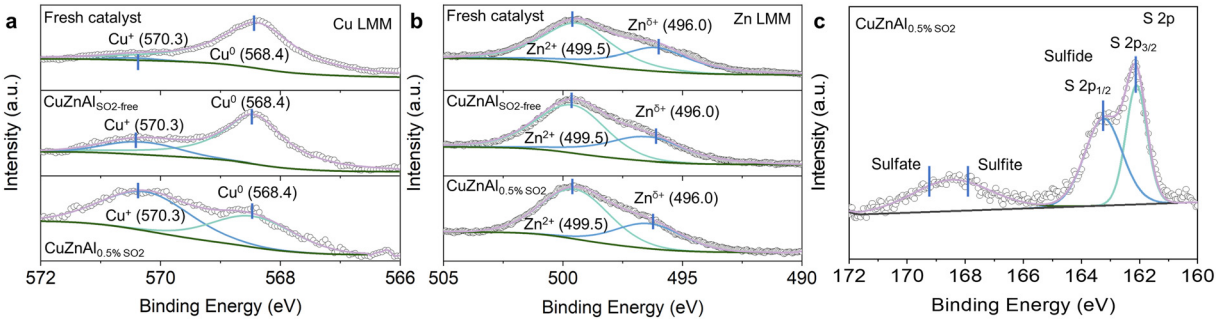

Fig. 3 Characterization of fresh and used Cu–ZnO–Al_2O_3 catalysts. (a) Cu LMM Auger spectra; (b) Zn LMM Auger spectra; (c) XPS spectra of S 2p. $CuZnAl_{SO_2\text{-free}}$: Cu–ZnO–$Al_2O_3$ exposed to $H_2/CO_2/N_2$ (1 : 1 : 1) for 400 min at 500 °C. $CuZnAl_{0.5\%SO_2}$: Cu–ZnO–Al_2O_3 exposed to $H_2/CO_2/N_2$ (1 : 1 : 1) with 0.5% SO_2 for 400 min at 500 °C.

S2†). These results suggest that both fresh and used catalysts maintain similar amount of $Zn^{\delta+}$, indicating that zinc remains predominantly in its oxidized state.

The S 2p spectra revealed the presence of sulfide (S 2p1/2 at 163.0 eV and S 2p3/2 at 162.1 eV), sulfates (at 169.2 eV) and sulfites (at 168.0 eV) species (Fig. 3c).[31,32] Notably, the content of sulfides was 67%, suggesting the majority of sulfur species on the surface of the used catalyst under 0.5% SO_2 condition were in the form of metal sulfides. Additionally, the Al 2p spectra displayed consistent signals across all three catalysts, indicating the stability of aluminum within the catalyst (Fig. S3†). The peak at 75.4 eV corresponded to Al 2p, while the shoulder peak at 78.1 eV was attributed to Cu 3p.[33–35]

Transmission electron microscopy (TEM) was used to investigate the changes in catalyst morphology (Fig. 4). The fresh catalyst exhibited a uniform distribution of Cu and ZnO nanoparticles, suggesting good dispersion and potential for high catalytic activity (Fig. 4a and S4†). For the catalyst used under SO_2-free conditions, no significant changes in particle size or morphology were observed, indicating that the catalyst remained stable under these conditions (Fig. 4b and S4†). However, upon exposure to 0.5% SO_2, sulfur was detected on the catalyst surface, indicating sulfur-induced sintering or poisoning effects (Fig. 4c and S4†). The observed changes in sulfur deposition could be linked to the decrease in catalytic activity under SO_2 exposure, as the sulfur species may interact with active sites and hinder CO_2 hydrogenation.

2.2.2 Effect of SO_2 on surface functional groups. To investigate the intermediates formed during CO_2 hydrogenation, *operando* DRIFTS was employed (Fig. 5). The catalyst was reduced *in situ* under a 5% H_2/N_2 flow at 500 °C for 2 h. The reaction gas, comprising CO_2, H_2, and N_2 in a 1 : 1 : 1 ratio, was then introduced to interact with the reduced catalyst at 500 °C. The bands observed at 1315 and 1455 cm^{-1} were attributed to carbonate species on the Cu–ZnO_x interface,[36–38] while no bands in the 3000–2400 cm^{-1} range were detected, indicating no formate species exist (Fig. 5a and S5†). Gas-phase CO was also identified with bands at 2177 and 2114 cm^{-1}.[37,39] During this process, the CO_2 conversion maintains at 27.5%, with the 100% CO selectivity (Fig. S5†).

Subsequently, the gas flow was switched to a 1 : 1 mixture of H_2 and CO_2 with 0.5% SO_2, and the reaction was monitored for 180 min (Fig. 5b). After 180 min, CO_2 conversion dropped from 27.5% to lower than 0.1%, indicating complete catalyst deactivation (Fig. S5†). At this point, the gas-phase CO bands (2177 and 2114 cm^{-1}) disappeared, suggesting a significant

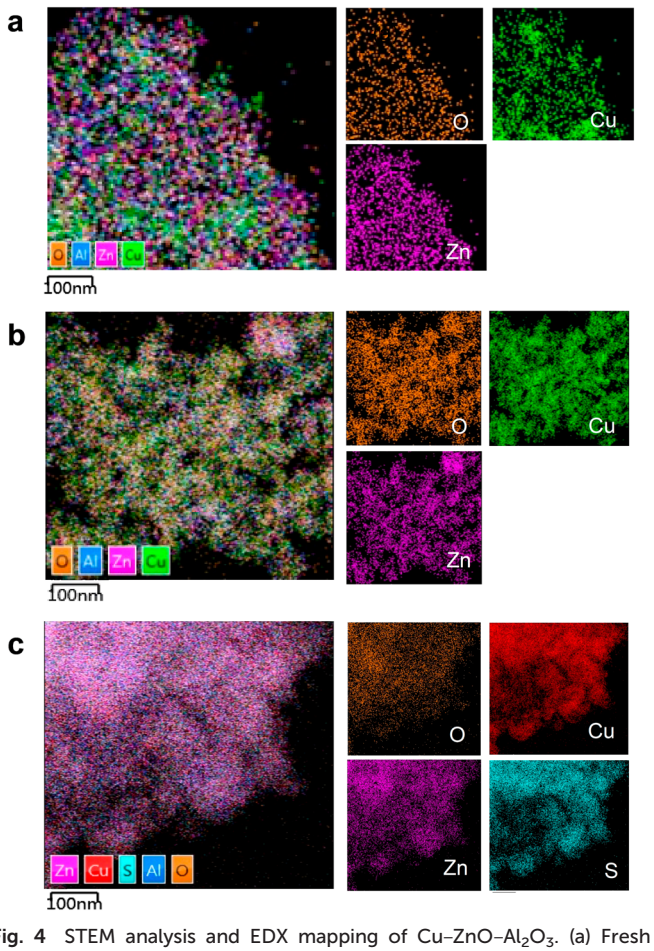

Fig. 4 STEM analysis and EDX mapping of Cu–ZnO–Al_2O_3. (a) Fresh catalyst; (b) the used catalyst exposed to $H_2/CO_2/N_2$ (1 : 1 : 1) for 400 min at 500 °C; (c) the used catalyst exposed to $H_2/CO_2/N_2$ (1 : 1 : 1) with 0.5% SO_2 for 400 min at 500 °C.

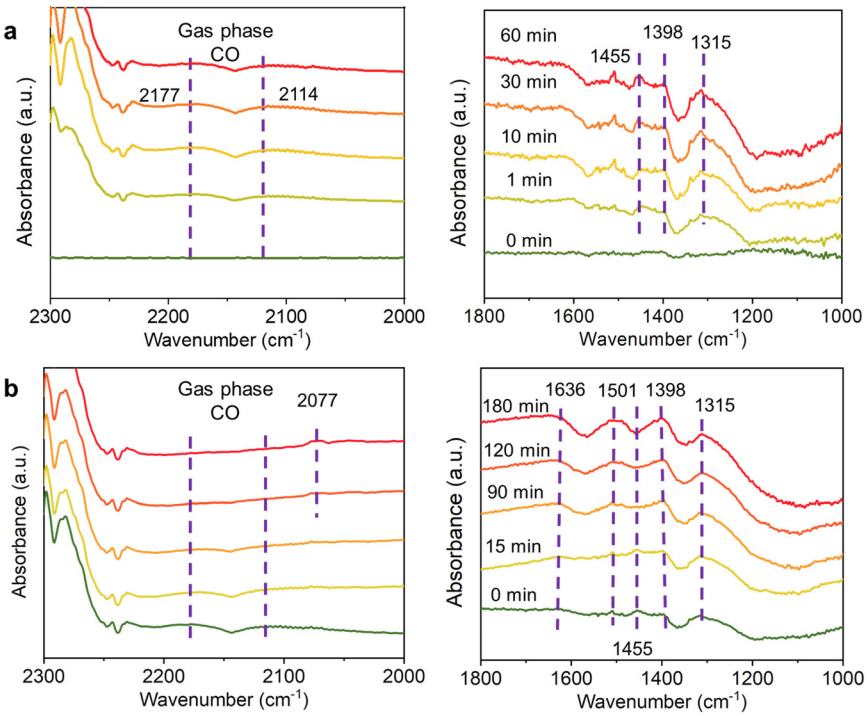

Fig. 5 *Operando* DRIFT spectra over the Cu–ZnO–Al_2O_3 catalyst under different feed gas compositions. The catalyst was first exposed to (a) CO_2/H_2/N_2 (1 : 1 : 1) for 60 min, followed by (b) switching the gas flow to CO_2/H_2/N_2 (1 : 1 : 1) with 0.5% SO_2. Reaction condition: 500 °C, 1 bar, and 30 mL min^{-1}, 0.5% SO_2.

reduction in CO formation. Additionally, a new band at 2077 cm^{-1} emerged, which is characteristic of carbonyl species,[40] indicating these species are not desorbing into the gas phase as CO. These carbonyl species are strongly adsorbed on the catalyst surface, likely due to strong interaction with active sites, making them difficult to desorb.

Moreover, the DRIFT spectra revealed the formation of new bands at 1401 and 1636 cm^{-1}, which are assigned to sulfate species, while the band at 1501 cm^{-1} is characteristic of sulfite species, respectively.[41–43] These findings indicate that SO_2 is strongly adsorbed onto the catalyst surface, predominantly in the form of sulfate and sulfite. The strong adsorption of these species leads to the occupation and blockage of the active sites, preventing the adsorption of reactants and ultimately inhibiting catalytic activity.[11,40,41] Consequently, the accumulation of these sulfur compounds accelerates catalyst deactivation, further exacerbating the decline in catalytic performance over time. Notably, the absence of characteristic bands in the 1211–1119 cm^{-1} region, which are typically associated with bulk sulfate species,[43–46] suggests that the sulfates formed during SO_2 exposure remain confined to the catalyst surface rather than incorporating into the bulk structure.

2.2.3 Effect of SO_2 on the crystal structure of the catalyst. XRD was employed to analyze phase changes in the catalysts under SO_2-free and 0.5% SO_2 conditions (Fig. 6). The XRD patterns of both the fresh catalyst and the catalyst under SO_2-free conditions revealed prominent peaks corresponding to

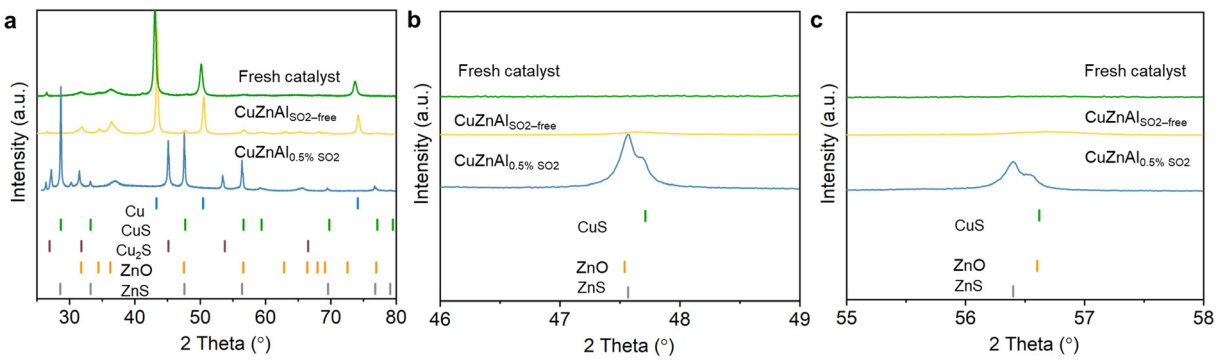

Fig. 6 XRD of the fresh and used catalysts with or without 0.5% SO_2. (a) XRD in the 2θ range of 25–80°; (b) XRD in the 2θ range of 46–49°; (c) XRD in the 2θ range of 55–58°.

Cu and ZnO (Fig. 6a). No discernible peaks for Al_2O_3 were observed, likely due to its low content, uniform distribution, and amorphous phase.[47] The peak at 26.5° was attributed to the (002) plane of graphite, commonly used as a binder in catalyst preparation.[48] Given the inert nature of graphite, its catalytic contribution is negligible and will not be discussed further.[49] Characteristic peaks at 43.3°, 50.4°, and 74.1° were identified, corresponding to the (111), (200), and (220) planes of metallic Cu (JCPDS 85-1326).[50] Peaks at 31.9°, 34.6°, 36.4°, 47.6°, 56.8°, 63.1°, and 68.2° were attributed to ZnO species (JCPDS 75-1526).[51,52] A slight shift in the diffraction peaks of Cu in the fresh catalyst indicated the formation of a CuZn alloy.[27,39] Additionally, the crystallite sizes for Cu and ZnO in industrial catalyst was measured as 27.0 nm and 17.5 nm, respectively. For the used catalyst under SO_2 free condition, the crystallite sizes for Cu and ZnO were 27.8 nm and 14.3 nm, respectively.

For the used catalyst under 0.5% SO_2 conditions, the peaks corresponding to metallic Cu disappeared, and new peaks at 26.6°, 30.8°, 44.1°, and 52.3° emerged, which were attributed to Cu_2S (JCPDS 75-2241).[53,54] New peaks at 27.9°, 47.5°, and 56.4° emerged, indicating the formation of either ZnS or CuS (JCPDS 01-0792 and 89-2073).[55,56] These peaks were located at similar positions, making it difficult to

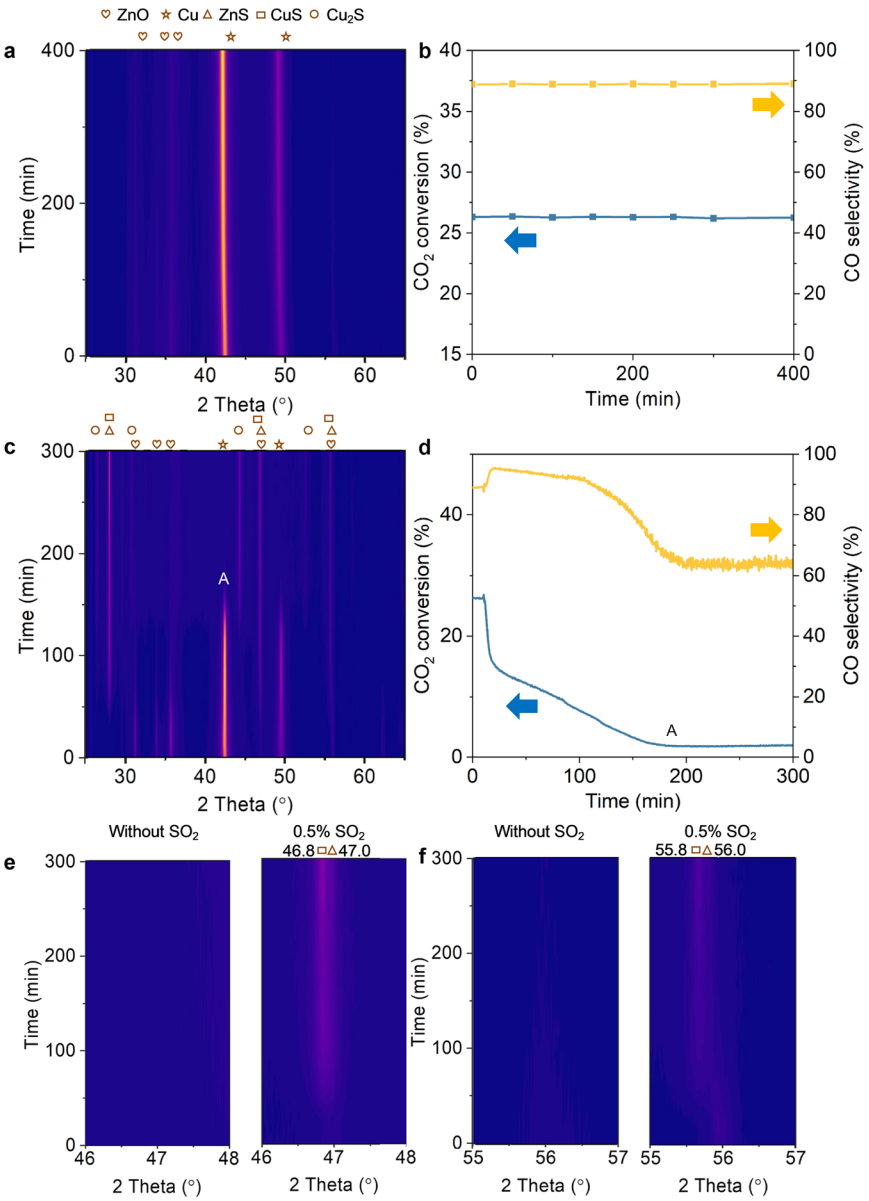

Fig. 7 *Operando* XRD over the Cu–ZnO–Al_2O_3 catalyst. (a) *Operando* XRD without SO_2 in the 2θ range of 25° to 65°; (b) CO_2 conversion and CO selectivity over 400 min of TOS under SO_2 free condition (reaction conditions: 500 °C, 1 bar, 150 mg catalyst loaded, $H_2:CO_2:N_2$ = 1 : 1 : 1, with a flow rate of 100 mL min^{-1}); (c) *operando* XRD under 0.5% SO_2 in the 2θ range of 25° to 65°; (d) CO_2 conversion and CO selectivity over 300 min of TOS under 0.5% SO_2 condition; (e) *operando* XRD under 0.5% SO_2 in the 2θ range of 45° to 48°; (f) *operando* XRD under 0.5% SO_2 in the 2θ range of 53° to 58° (reaction condition: 1 bar, 500 °C, 150 mg catalyst loaded, $CO_2/H_2/N_2$ (1 : 1 : 1) with 0.5% SO_2, with a flow rate of 100 mL min^{-1}).

distinguish between CuS and ZnS. Moreover, it was not possible to unequivocally assign the peaks at 47.5° and 56.4° to either newly formed metal sulfides or to ZnO (Fig. 6b and c). To clarify these ambiguities, *operando* XRD measurements were conducted. Moreover, the crystallite size for Cu_2S was 49.5 nm, overlapping peaks for CuS and ZnS suggest a composite crystallite size of 67.9 nm, though this value should be interpreted cautiously due to peak overlap. The growth of the particle sizes indicates that SO_2 exposure induces moderate crystallite growth in Cu-derived sulfides (Cu_2S/CuS) and ZnS, likely driven by phase restructuring during sulfidation.

The catalytic behavior of Cu–ZnO–Al_2O_3 catalysts during CO_2 hydrogenation was investigated using *operando* XRD analysis under both SO_2-free and 0.5% SO_2 conditions (Fig. 7). Under SO_2-free conditions, characteristic peaks corresponding to Cu (42.5° and 49.4°) and ZnO (31.1°, 34.0°, and 35.6°) were observed (Fig. 7a). These peaks exhibited slight shifts to lower 2θ values compared to the *ex situ* XRD at room temperature, which can be attributed to the lattice expansion at elevated temperatures. Over a time-on-stream (TOS) of 400 min, the catalyst retained its original structure, with XRD patterns displaying consistent peaks for Cu, ZnO, and Al_2O_3, without significant shifts in peak positions or intensities. It is worth noting that the ZnO peaks (47.0° and 56.0°) were not as pronounced, likely due to the high intensity of the Cu peaks. Throughout the reaction, CO_2 conversion and CO selectivity remained stable at 26.3% and 88.9%, respectively (Fig. 7b).

Upon introducing SO_2 into the reaction environment, significant changes in the structure and catalytic properties were observed (Fig. 7c). Catalytic performance was continuously monitored using a gas analyzer (Fig. 7d). X-ray diffraction (XRD) analysis revealed a gradual decrease in the intensity of the ZnO peaks at 31.1°, 34.0°, and 35.6°, as well as a decrease in the intensity of the Cu peaks at 42.5° and 49.5°. Meanwhile, new peaks corresponding to metal sulfides appeared and became more pronounced at 27.9°, 46.8°,47.0 55.8° and 56.0.

Both ZnS and CuS exhibit peaks at similar positions in the XRD patterns. According to the standard PDF cards, CuS has characteristic peaks at 28.7°, 47.7°, and 56.6°, whereas ZnS displays peaks at 28.6°, 47.5°, and 56.4°. Based on these values, the peaks observed at 46.8° and 47.0° are assigned to CuS and ZnS, respectively, while the peaks at 55.8° and 56.0° are attributed to CuS and ZnS, respectively (Fig. 7e and f). Notably, prior to the introduction of SO_2, the peaks at 47.0° and 56.0° were weak or absent, suggesting that the newly intensified peaks at these positions after SO_2 exposure do not correspond to ZnO. Instead, the weakening of other ZnO peaks supports the assignment of these new peaks to metal sulfides, indicating the formation of CuS and ZnS as a result of SO_2-induced catalyst deactivation. Additionally, the peak at 27.9° is attributed to a mixture of CuS and ZnS.

The formation of CuS and ZnS was accompanied by a significant decrease in CO_2 conversion. Combining the phase transitions with the catalytic performance, we observed that after the introduction of SO_2 into the flow for 10 min, metal sulfides began to form, and CO_2 conversion started to decline. Meanwhile, CO selectivity increased due to the rapid decrease in CH_4 formation, exhibiting trends similar to those observed in the fixed-bed reactor (Fig. 7d).

Subsequently, XRD analysis showed the disappearance of metallic Cu at point A, accompanied by the appearance of three new peaks at 30.8°, 44.5°, and 52.6°, which were attributed to Cu_2S. At this point, the catalyst exhibited complete deactivation. This indicates that the gradual decrease in CO_2 conversion was linked to the formation of metal sulfides and the disappearance of metallic Cu. The full conversion of ZnO and Cu into metal sulfides led to catalyst deactivation. Notably, no sulfates or sulfites were detected during the process.[57–59] It is important to note that in the *operando* XRD setup, the contact time is 0.09 s g mL^{-1}, whereas in the quartz tube reactor, the contact time is shorter at 0.05 s g mL^{-1}. The longer contact time in the *operando* XRD experiment leads to a more prolonged interaction between the catalyst and reactants or poisons, which accelerates the accumulation of these species on the catalyst surface. This may result in faster catalyst deactivation. Therefore, although the catalyst in the quartz tube reactor eventually reaches full deactivation, some residual zero-valent copper remains detectable (shown in the XPS result, Fig. 3a) due to the shorter contact time and lower accumulation of reaction products and poisons.

We then performed a detailed kinetic analysis of the time-dependent XRD data. Due to the overlapping characteristic peaks of ZnS and CuS in the low-angle region ($2\theta \leq 0.2°$), it is challenging to unambiguously distinguish these sulfide phases solely *via* XRD. To address this limitation, our kinetic analysis focuses on the disappearance of the metallic Cu and ZnO phases, which exhibit distinct and non-overlapping diffraction signatures. This semi-quantitative approach tracks the decay of the reactant phases (Cu and ZnO) rather than directly quantifying the sulfide products (CuS/Cu_2S and ZnS), providing robust insights into the sulfidation kinetics while mitigating phase deconvolution uncertainties.

For Cu-to-CuS/Cu_2S transformation (Fig. S6†), a power-law logistic function (eqn (1)) captures a three-stage diffusion-controlled mechanism: (1) a lag phase (0–15 min) with slow nucleation due to sulfur incorporation barriers, (2) a growth phase (15–60 min) dominated by accelerated 3D sulfur diffusion into the Cu lattice, and (3) a saturation phase (>60 min) where unreacted Cu is kinetically trapped within a core-shell structure. In contrast, ZnO-to-ZnS conversion (Fig. S7†) follows a single-exponential decay model (eqn (2)), revealing a two-phase process: (1) an initial fast phase (0–30 min) driven by rapid surface reactions between ZnO and sulfur sources, and (2) a slow phase (>30 min) limited by ZnS passivation layer formation, which impedes bulk diffusion. These analyses collectively highlight how material-specific properties—Cu's metallic lattice favoring diffusion-limited nucleation-growth *versus* ZnO's semiconductor surface reactivity—govern sulfidation kinetics.

$$X(t) = 0.64 + 96.68/\left(1 + \left(\frac{t}{27.3}\right)^{3.8}\right) \quad (1)$$

$$X(t) = 103.8e^{-\frac{t}{26.3}} + 1.08 \quad (2)$$

Hydrogen temperature-programmed reduction (H_2-TPR) analysis was conducted on Cu–ZnO–Al_2O_3 catalysts under different conditions (Fig. 8 and Table S3†). For the industrial catalyst, two distinct reduction peaks were observed at 201 and 282 °C, corresponding to the reduction processes from CuO to Cu_2O and from Cu_2O to Cu, respectively (Fig. 8a). The total hydrogen consumption was 155 μmol g^{-1} (Fig. 8b). In contrast, for the catalyst subjected to CO_2 hydrogenation treatment without SO_2 exposure, the peak at 278 °C remained, but the total hydrogen consumption decreased to 143 μmol g^{-1}, which was comparable to that of the fresh catalyst. The peak at 278 °C indicates the presence of Cu^+ species, with no Cu^{2+} detected, consistent with the XRD and XPS results. For the used catalyst exposed to SO_2, a dramatic decrease in hydrogen consumption was observed. The H_2-TPR profile showed a single reduction peak at 150 °C, with only 10 μmol g^{-1} of hydrogen consumption, highlighting a significant loss in reducibility. This result implies that SO_2 exposure induces the formation of metal sulfides, which strongly inhibit the reduction of the active sites, leading to catalyst deactivation. The absence of higher temperature reduction peaks (at 201 °C and 280 °C) suggests that all Cu species have been converted to metal sulfides, preventing further reduction and impairing catalytic performance.

To probe the spatial distribution of deactivated catalytic sites, H_2-TPD analysis was conducted (Fig. 8c). H_2-TPD reveals that the number of H_2-adsorbing active sites (attributed to metallic Cu) sharply decreases in the presence of SO_2. Specifically, the H_2 uptake drops from 83 μmol g^{-1} (fresh catalyst) and 78 μmol g^{-1} (post-reaction without SO_2) to nearly zero under SO_2-containing conditions (Fig. 8d). This aligns with the complete loss of catalytic activity, confirming that SO_2-induced sulfidation fully converts surface Cu sites into inactive sulfur-containing species (whether as sulfides, sulfates, or sulfites), thereby irreversibly deactivating the catalyst.

Inductively coupled plasma optical emission spectrometer (ICP-OES) was used to identify the sulfur content in the used catalyst (Table S3†). The experimental sulfur content of 235.3 mg g^{-1} (~33.5 wt%), lying between the theoretical thresholds for complete Cu→Cu_2S (26.3 wt%) and Cu→CuS (41.2 wt%) conversions, strongly indicates a mixed sulfide phase composition. This intermediate sulfur uptake demonstrates that copper species undergo partial sulfidation to both Cu_2S and CuS, while zinc predominantly forms ZnS as evidenced by its stoichiometric sulfur demand. The quantitative alignment with sulfide-phase predictions, coupled with XRD identification of crystalline Cu_2S/CuS and ZnS phases, confirms that irreversible deactivation originates from bulk sulfide formation rather than surface adsorption. This mechanistic interpretation is further corroborated by

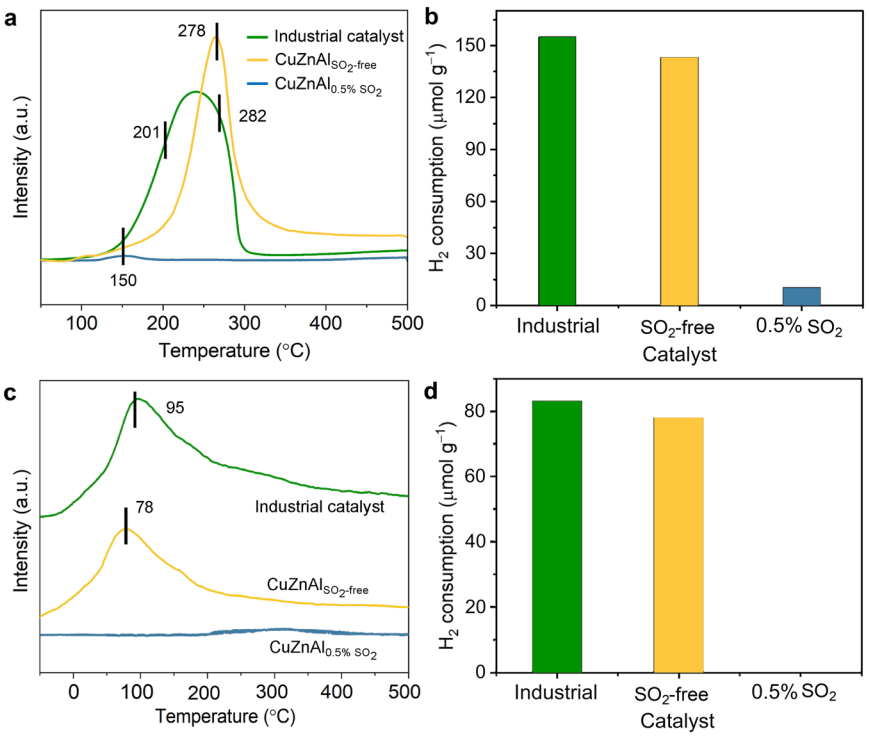

Fig. 8 H_2-TPR (a and b) and H_2-TPD (c and d) of the fresh catalyst and the used catalysts under CO_2 hydrogenation condition with or without 0.5% SO_2. The used catalysts were treated using $H_2/CO_2/N_2$ (1 : 1 : 1) with or without 0.5% SO_2 for 400 min at 500 °C.

H_2-TPD results showing near-complete loss of hydrogen adsorption capacity, consistent with sulfide-induced active site blockage at both surface and subsurface levels.

2.3 Discussion

XPS analysis showed that Cu predominantly exists as Cu^+ ions, along with the presence of metal sulfides, sulfate, and sulfite species. *Operando* DRIFTS further confirmed the presence of these sulfur species by showing characteristic peaks for sulfates and sulfites. However, no sulfate or sulfite signals were detected in the bulk phase, suggesting that these species are exclusively formed on the surface.

Referring to the previous studies on the effect of SO_2 on NH_3-SCR response and ICCU,[23,25,26,60–62] the deactivation mechanisms induced by SO_2 in NH_3-SCR systems and CO_2 hydrogenation processes exhibit fundamental differences due to their distinct reaction environments. In NH_3-SCR systems operating under oxidizing conditions (with flue gas containing O_2), SO_2 oxidation is strongly promoted, leading to the predominant formation of ammonium sulfate and surface-adsorbed sulfates/sulfites.[25,60–62] These species progressively block active sites and deplete catalytically active Cu species through bulk sulfate formation. In contrast, CO_2 hydrogenation process contains the weakly oxidizing species CO_2 and strongly reducing sepcies H_2. Thermodynamic calculations ($\Delta G < 0$ at elevated temperatures, Fig. S8†) and experimental evidence demonstrate that H_2 drives the reduction of SO_2 to H_2S (Fig. S9†), which subsequently reacts with catalyst components to form bulk metal sulfides (CuS, Cu_2S, ZnS). Furthermore, parallels emerge when comparing SO_2 interactions in CO_2 capture systems due to the presence of O_2 5,6. For instance, in ICCU processes,[23,26] SO_2 exposure under oxidative conditions rapidly converts CaO to thermally stable $CaSO_4$, significantly degrading CO_2 capture capacity due to pore blockage and mass transfer limitations. This underscores the universal challenge of sulfur poisoning across systems, while emphasizing that the dominant sulfur species (sulfates *vs.* sulfides) are dictated by the local chemical environment—oxidizing conditions favor sulfation, whereas reducing conditions drive sulfidation.

The surface sulfur speciation analysis by XPS reveals an intriguing distribution pattern: sulfates and sulfites collectively account for only 33% of surface sulfur species, with sulfides constituting the majority. This observation can be rationalized through three key factors: (1) the absence of gaseous O_2 restricts sulfite formation to ZnO vicinal sites through Zn–O–SO_2 interactions; (2) sulfate generation requires dual participation of metal oxides and reactive oxygen species derived from CO_2 activation, imposing strict spatial constraints; (3) dynamic interconversion between sulfur species under reaction conditions. Literature reports indicate sulfites exhibit thermal lability (decomposition >200 °C), while sulfates demonstrate higher stability (decomposition >650 °C).[63–65] Crucially, in the H_2-rich environment, both sulfites and sulfates undergo progressive reduction to sulfides, establishing a cyclic transformation pathway (sulfites ↔ sulfates → sulfides).

Exposure to SO_2 leads to a gradual decline in catalytic activity. Partial recovery is observed in the short term, but prolonged exposure results in irreversible deactivation, with no recovery after complete deactivation. The partial reversibility observed during transient H_2S exposure likely arises from incomplete poisoning due to insufficient sulfidation time, allowing the decomposition of sulfites/sulfites to release the active sites. However, once full bulk sulfidation is achieved (confirmed by XRD), the deactivation becomes irreversible, with no significant activity recovery. XRD results indicate that complete deactivation occurs after Cu and ZnO are transformed into CuS, Cu_2S, and ZnS phases, confirming the catalytic inactivity of these bulk sulfides. The short-term recovery of activity is attributed to the residual catalytic activity of un-sulfidized material. However, once a complete phase transformation occurs, catalytic activity cannot be restored. Together, these findings highlight the detrimental effects of SO_2 on the catalyst, emphasizing the need for developing sulfur-resistant catalysts or advanced sulfur-removal methods. These insights are critical for improving the durability of CO_2 hydrogenation processes under industrial conditions.

3 Conclusions

This study systematically investigated the impact of SO_2 on the structural and catalytic properties of Cu–ZnO–Al_2O_3 catalysts. The results revealed that SO_2 exposure induces significant changes in the catalyst composition, leading to substantial deactivation. Specifically, sulfates and sulfites are adsorbed on the catalyst surface blocking active sites and impairing catalytic performance. This is further corroborated by the formation of metal carbonyl species, indicating that sulfur species hinder the desorption of CO. In addition, SO_2 exposure caused the progressive transformation of Cu and Zn into catalytically inactive metal sulfides (CuS, Cu_2S, and ZnS). Overall, the combined effects of metal sulfide formation and surface sulfate/sulfite accumulation significantly reduce catalytic activity, underscoring the detrimental role of SO_2 in catalyst deactivation. These findings provide critical insights into the mechanisms of SO_2-induced catalyst poisoning, which are essential for developing sulfur-tolerant catalysts for CO_2 hydrogenation under industrial conditions.

4 Experimental section

4.1 Materials

The industrial Cu–ZnO–Al_2O_3 catalyst used in this study was purchased from Tianjin Kaite New Material Technology Co., Ltd. The concentrations of Cu, ZnO, and Al_2O_3 in the catalysts were 59.1%, 29.0%, and 11.9%, respectively, as determined by ICP-OES (iCAP 7400, Thermo Fisher, Table S3†).

4.2 CO_2 hydrogenation

The CO_2 hydrogenation reactions were carried out in a fixed-bed quartz reactor with an inner diameter of 6 mm. The

catalyst (0.05 g) was loaded into the reactor and held in place with quartz wool. The reactor was connected to a gas feed system that allowed precise control over the flow rates of CO_2, H_2, and SO_2. Before the catalytic tests, the Cu–ZnO–Al_2O_3 catalyst was reduced *in situ* at 500 °C in a 5% H_2/N_2 flow for 2 h to generate the active metallic Cu phase. The reaction gas mixture was passed through the reactor at a total flow rate of 60 mL min^{-1}, and the pressure inside the reactor was maintained at 1 bar. The reaction was conducted at a temperature range from 300–700 °C, and the products were analyzed using a Gasboard 3100 Gas Analyzer (Hubei Ruiyi Co., Ltd). The catalyst was exposed to different concentrations of SO_2 (ranging from 0 to 2%) in the CO_2/H_2 (1 : 1) gas mixture to evaluate the effect of SO_2 on the catalytic performance. For each condition, the experiment was repeated three times to ensure reproducibility.

4.3 Catalyst characterization

STEM with energy-dispersive X-ray (EDX) spectroscopy was carried out using a high-resolution field emission TEM (JEM-2100F), which features advanced drift correction technology. The instrument was operated at an electron acceleration voltage of 200 kV, offering a point resolution of 0.23 nm and a scanning transmission electron microscopy (STEM) resolution of 0.20 nm. The lattice resolution achieved was 0.10 nm, enabling detailed elemental analysis across a broad spectrum, from beryllium (Be, atomic number 4) to uranium (U, atomic number 92). Molybdenum grids were employed to prevent interference from copper scattering.

Powder XRD analysis was performed using a PANalytical Empyrean series diffractometer equipped with a high-definition Bragg–Brentano mirror. The instrument operated at 45 kV and 40 mA, utilizing Cu Kα radiation (λ = 1.5406 Å). Data were collected within a 2θ range of 5–90° with scanning speed of 0.013° per step. *Operando* XRD experiments were performed in PANalytical Empyrean series diffractometer equipped with reactor chamber XRK 900 from Anton Paar. The collected 2 theta range is 25–65° with scanning speed of 0.013° and 42 second per step. The sample was pre-reduced in 5% H_2/N_2 stream (100 mL min^{-1}) at 500 °C for 2 h. After reduction, the sample were in the different flow by 100 mL min^{-1} CO_2/H_2 (1 : 1) or CO_2/H_2 with 0.5% SO_2 under 500 °C for different min. The XRD patterns were recorded continuously for all stages.

XPS was carried out with an ESCALAB Xi+ instrument (Thermo Fisher Scientific) in an ultra-high vacuum environment (less than 1.0×10^{-9} mbar). A monochromatic Al target and magnetic lens mode were used, with a 500 μm X-ray beam spot. Survey spectra were recorded with a pass energy of 160 eV and a step size of 1.0 eV, while narrow scan spectra were recorded at a pass energy of 20 eV and a step size of 0.05 eV. Samples, supported on carbon tapes, were transferred from the glovebox to the XPS chamber *via* an air-tight cell, ensuring no exposure to air.

H_2-TPR was carried out using a Micromeritics AutoChem 2920 instrument equipped with a thermal conductivity detector (TCD). Approximately 100 mg of sample was placed in a U-shaped quartz reactor. Prior to measurements, the sample was dried in an argon flow at 300 °C for 30 min with a heating rate of 10 °C min^{-1}. H_2-TPR was conducted under a 5% H_2/Ar mixture, heating from room temperature to 500 °C at a rate of 10 °C min^{-1}.

DRIFTS measurements were carried out using a Nicolet 6700 FTIR spectrometer, equipped with a mercury cadmium telluride detector. *Operando* DRIFT spectra were recorded with 32 scans at a resolution of 4 cm^{-1}. Prior to measurements, the catalysts were pretreated *in situ* with a 30 ml min^{-1} flow of 5% H_2 at 500 °C for 2 h. Background spectra were recorded at the same temperature under a nitrogen flow. Following this, the catalysts were exposed to a gas flow with the desired composition, maintained at a constant flow rate of 30 ml min^{-1} at the required temperature.

Data availability

The data that support the findings of this study are available from the corresponding author upon reasonable request.

Author contributions

H. Z. and X. B. conceived the research project. X. B. designed the experimental work. R. W. performed the CO_2 hydrogenation experiments. B. Y. contributed to the operando XRD experiments. S. Z. and X. Q. assisted with the catalyst characterization. Q. L. and Y. Z. supported the CO_2 hydrogenation reactions. Data analysis and interpretation were discussed among all coauthors. X. B. and H. Z. wrote the manuscript, with contributions from all authors.

Conflicts of interest

There are no conflicts to declare.

Acknowledgements

This work was supported by the Beijing Natural Science Foundation (JQ24053), National Natural Science Foundation of China (52276202), International Joint Mission on Climate Change and Carbon Neutrality, Natural Science Foundation of Shanxi Province (202403021211024, 202403021212148), and Tsinghua University Initiative Scientific Research Program.

References

1 L. J. R. Nunes, The rising threat of atmospheric CO_2: A review on the causes, impacts, and mitigation strategies, *Environments*, 2023, **10**, 1–22.
2 M. Ramonet, A. Chatterjee, P. Ciais, I. Levin, M. K. Sha, M. Steinbacher and C. Sweeney, *CO_2 in the atmosphere: Growth and trends since 1850*, Oxford University Press, 2023.
3 Z. Yang, R. Chen, L. Zhang, Y. Li and C. Li, Recent progress in nickel single-atom catalysts for the electroreduction of CO_2 to CO, *Ind. Chem. Mater.*, 2024, **2**, 533–555.

4 J. Hu, L. Yu, J. Deng, Y. Wang, K. Cheng, C. Ma, Q. Zhang, W. Wen, S. Yu, Y. Pan, J. Yang, H. Ma, F. Qi, Y. Wang, Y. Zheng, M. Chen, R. Huang, S. Zhang, Z. Zhao, J. Mao, X. Meng, Q. Ji, G. Hou, X. Han, X. Bao, Y. Wang and D. Deng, Sulfur vacancy-rich MoS_2 as a catalyst for the hydrogenation of CO_2 to methanol, *Nat. Catal.*, 2021, **4**, 242–250.

5 M. D. Porosoff, B. Yan and J. G. Chen, Catalytic reduction of CO_2 by H_2 for synthesis of CO, methanol and hydrocarbons: Challenges and opportunities, *Energy Environ. Sci.*, 2016, **9**, 62–73.

6 S. Wang, L. Zhang, P. Wang, W. Jiao, Z. Qin, M. Dong, J. Wang, U. Olsbye and W. Fan, Highly selective hydrogenation of CO_2 to propane over $GaZrO_x$/H-SSZ-13 composite, *Nat. Catal.*, 2022, **5**, 1038–1050.

7 H. Zhou, Z. Chen, A. V. López, E. D. López, E. Lam, A. Tsoukalou, E. Willinger, D. A. Kuznetsov, D. Mance, A. Kierzkowska, F. Donat, P. M. Abdala, A. Comas-Vives, C. Copéret, A. Fedorov and C. R. Müller, Engineering the Cu/Mo_2CT_x (MXene) interface to drive CO_2 hydrogenation to methanol, *Nat. Catal.*, 2021, **4**, 860–871.

8 H. Zhou, Z. Chen, E. Kountoupi, A. Tsoukalou, P. M. Abdala, P. Florian, A. Fedorov and C. R. Müller, Two-dimensional molybdenum carbide 2D-Mo_2C as a superior catalyst for CO_2 hydrogenation, *Nat. Commun.*, 2021, **12**, 5510.

9 S. Saeidi, S. Najari, V. Hessel, K. Wilson, F. J. Keil, P. Concepción, S. L. Suib and A. E. Rodrigues, Recent advances in CO_2 hydrogenation to value-added products—Current challenges and future directions, *Prog. Energy Combust. Sci.*, 2021, **85**, 100905.

10 S. Sun, Y. Wang, Y. Xu, H. Sun, X. Zhao, Y. Zhang, X. Yang, X. Bie, M. Wu, C. Zhang, Y. Zhu, Y. Xu, H. Zhou and C. Wu, Ni-functionalized Ca@Si yolk-shell nanoreactors for enhanced integrated CO_2 capture and dry reforming of methane via confined catalysis, *Appl. Catal., B*, 2024, **348**, 123838.

11 M. Zhang, X. Lu, K. Luo, J. Ye, J. L. Dong, N. Lu, X. Wang, Q. Niu, P. Zhang and S. Dai, High entropy oxide catalysts with SO_2 resistance in RWGS reaction, *Appl. Catal., B*, 2024, **349**, 123845.

12 N. Sadokhina, G. Smedler, U. Nylén, M. Olofsson and L. Olsson, Deceleration of SO_2 poisoning on $PtPd/Al_2O_3$ catalyst during complete methane oxidation, *Appl. Catal., B*, 2018, **236**, 384–395.

13 L. Kang, L. Han, J. He, H. Li, T. Yan, G. Chen, J. Zhang, L. Shi and D. Zhang, Improved NO_x reduction in the presence of SO_2 by using Fe_2O_3-promoted halloysite-supported CeO_2–WO_3 catalysts, *Environ. Sci. Technol.*, 2019, **53**, 938–945.

14 M. Pasichnyk, P. Stanovsky, P. Polezhaev, B. Zach, M. Šyc, M. Bobák, J. C. Jansen, M. Přibyl, J. E. Bara, K. Friess, J. Havlica, D. L. Gin, R. D. Noble and P. Izák, Membrane technology for challenging separations: Removal of CO_2, SO_2 and NO_x from flue and waste gases, *Sep. Purif. Technol.*, 2023, **323**, 124436.

15 J. Xie, D. Wang, L. Liu, T. Shao, H. Zhou and D. Zhang, An overview of flue gas so_2 capture technology based on absorbent evaluation and process intensification, *Ind. Eng. Chem. Res.*, 2024, **63**, 6066–6086.

16 Z. Zhu and B. Xu, Purification technologies for NO_x removal from flue gas: A review, *Separations*, 2022, **9**, 307.

17 R. T. J. Porter, M. Fairweather, M. Pourkashanian and R. M. Woolley, The range and level of impurities in CO_2 streams from different carbon capture sources, *Int. J. Greenhouse Gas Control*, 2015, **36**, 161–174.

18 A. Wang and L. Olsson, Insight into the SO_2 poisoning mechanism for NO_x removal by NH_3-SCR over Cu/LTA and Cu/SSZ-13, *Chem. Eng. J.*, 2020, **395**, 125048.

19 L. Liu, S. Su, D. Chen, T. Shu, X. Zheng, J. Yu, Y. Feng, Y. Wang, S. Hu and J. Xiang, Highly efficient NH_3-SCR of NO over MnFeW/Ti catalyst at low temperature: SO_2 tolerance and reaction mechanism, *Fuel*, 2022, **307**, 121805.

20 J. Chen, Y. Xu, P. Liao, H. Wang and H. Zhou, Recent progress in integrated CO_2 capture and conversion process using dual function materials: A state-of-the-art review, *Carbon Capture Sci. Technol.*, 2022, **4**, 100052.

21 L. Zhu, J. Yao, G. Ma, P. Cao, S. Wu and Z. Li, NH_3-SCR performance and SO_2 resistance comparison of CeO_2 based catalysts with Fe/Mo additive surface decoration, *Chem. Eng. J.*, 2022, **428**, 131372.

22 R. Purbia, S. Y. Choi, H. J. Kim, B. Ye, B. Jeong, D. H. Lee, H. Park, H.-D. Kim and J. M. Baik, Cu- and Ce-promoted nano-heterostructures on vanadate catalysts for low-temperature NH_3–SCR activity with improved SO_2 and water resistance, *Chem. Eng. J.*, 2022, **437**, 135427.

23 X. Xie, L. Liu, H. Liu and Z. Sun, Mechanistic insights into SO_2-induced deactivation of Ni-based materials for integrated CO_2 capture and methanation, *Fuel*, 2025, **382**, 133755.

24 H. Zhou, S. Sun, Y. Xu, Y. Zhang, S. Yi and C. Wu, Upcycling municipal solid waste to sustainable hydrogen via two-stage gasification-reforming, *J. Energy Chem.*, 2024, **96**, 611–624.

25 K. Wijayanti, K. Xie, A. Kumar, K. Kamasamudram and L. Olsson, Effect of gas compositions on SO_2 poisoning over Cu/SSZ-13 used for NH_3-SCR, *Appl. Catal., B*, 2017, **219**, 142–154.

26 S. Cimino, E. M. Cepollaro and L. Lisi, Ageing study of Li-Ru/Al_2O_3 dual function material during the integrated CO_2 capture and methanation with SO_2-containing flue gas, *Carbon Capture Sci. Technol.*, 2023, **6**, 100096.

27 H. Zhou, S. R. Docherty, N. Phongprueksathat, Z. Chen, A. V. Bukhtiyarov, I. P. Prosvirin, O. V. Safonova, A. Urakawa, C. Copéret, C. R. Müller and A. Fedorov, Combining atomic layer deposition with surface organometallic chemistry to enhance atomic-scale interactions and improve the activity and selectivity of Cu–Zn/SiO_2 catalysts for the hydrogenation of CO_2 to methanol, *JACS Au*, 2023, **3**, 2536–2549.

28 R. Ye, L. Ma, J. Mao, X. Wang, X. Hong, A. Gallo, Y. Ma, W. Luo, B. Wang, R. Zhang, M. S. Duyar, Z. Jiang and J. Liu, A Ce-CuZn catalyst with abundant Cu/Zn-O_V-Ce active sites for CO_2 hydrogenation to methanol, *Nat. Commun.*, 2024, **15**, 2159.

29 S. Kuld, C. Conradsen, P. G. Moses, I. Chorkendorff and J. Sehested, Quantification of zinc atoms in a surface alloy on copper in an industrial-type methanol synthesis catalyst, *Angew. Chem., Int. Ed.*, 2014, **53**, 5941–5945.

30 D. Li, F. Xu, X. Tang, S. Dai, T. Pu, X. Liu, P. Tian, F. Xuan, Z. Xu, I. E. Wachs and M. Zhu, Induced activation of the commercial Cu/ZnO/Al_2O_3 catalyst for the steam reforming of methanol, *Nat. Catal.*, 2022, **5**, 99–108.
31 V. V. Mesilov, S. L. Bergman, S. Dahlin, Y. Xiao, S. Xi, M. Zhirui, L. Xu, W. Chen, L. J. Pettersson and S. L. Bernasek, Differences in oxidation-reduction kinetics and mobility of Cu species in fresh and SO_2-poisoned Cu-SSZ-13 catalysts, *Appl. Catal., B*, 2021, **284**, 119756.
32 X. Pang, W. Liu, H. Xu, Q. Hong, P. Cui, W. Huang, Z. Qu and N. Yan, Selective uptake of gaseous sulfur trioxide and mercury in ZnO-CuS composite at elevated temperatures from SO_2-rich flue gas, *Chem. Eng. J.*, 2022, **427**, 132035.
33 J. Li, M. Li, C. Zhang, C. L. Liu, R. Z. Yang and W. S. Dong, Construction of mesoporous Cu/ZrO_2-Al_2O_3 as a ternary catalyst for efficient synthesis of γ-valerolactone from levulinic acid at low temperature, *J. Catal.*, 2020, **381**, 163–174.
34 A. Venugopal, J. Palgunadi, J. K. Deog, O. S. Joo and C. H. Shin, Dimethyl ether synthesis on the admixed catalysts of Cu-Zn-Al-M (M = Ga, La, Y, Zr) and γ-Al_2O_3: The role of modifier, *J. Mol. Catal. A:Chem.*, 2009, **302**, 20–27.
35 R. Ahmad, M. Hellinger, M. Buchholz, H. Sezen, L. Gharnati, C. Wöll, J. Sauer, M. Döring, J.-D. Grunwaldt and U. Arnold, Flame-made Cu/ZnO/Al_2O_3 catalyst for dimethyl ether production, *Catal. Commun.*, 2014, **43**, 52–56.
36 A. Beck, M. Zabilskiy, M. A. Newton, O. Safonova, M. G. Willinger and J. A. Van Bokhoven, Following the structure of copper-zinc-alumina across the pressure gap in carbon dioxide hydrogenation, *Nat. Catal.*, 2021, **4**, 488–497.
37 H. Zhang, J. Chen, X. Han, Y. Pan, Z. Hao, S. Tang, X. Zi, Z. Zhang, P. Gao, M. Li, J. Lv and X. Ma, High-performance Cu/ZnO/Al_2O_3 catalysts for CO_2 hydrogenation to methanol, *Ind. Eng. Chem. Res.*, 2024, **63**, 6210–6221.
38 M. Behrens, F. Studt, I. Kasatkin, S. Kühl, M. Hävecker, F. Abild-Pedersen, S. Zander, F. Girgsdies, P. Kurr, B.-L. Kniep, M. Tovar, R. W. Fischer, J. K. Nørskov and R. Schlögl, The active site of methanol synthesis over Cu/ZnO/Al_2O_3 industrial catalysts, *Science*, 2012, **336**, 893–897.
39 X. Bie, Y. Pan, X. Wang, S. Zhang, J. Hu, X. Yang, Q. Li, Y. Zhang, R. E. Przekop, Y. Zhang and H. Zhou, NH_3-induced challenges in CO_2 hydrogenation over the Cu/ZnO/Al_2O_3 catalyst, *JACS Au*, 2025, **5**, 1243–1257.
40 J. Schumann, J. Kröhnert, E. Frei, R. Schlögl and A. Trunschke, IR-spectroscopic study on the interface of Cu-based methanol synthesis catalysts: Evidence for the formation of a ZnO overlayer, *Top. Catal.*, 2017, **60**, 1735–1743.
41 P. A. Kumar, Y. E. Jeong, S. Gautam, H. P. Ha, K. J. Lee and K. H. Chae, XANES and DRIFTS study of sulfated Sb/V/Ce/TiO_2 catalysts for NH_3-SCR, *Chem. Eng. J.*, 2015, **275**, 142–151.
42 Q. Wu, H. Gao and H. He, Conformational analysis of sulfate species on Ag/Al_2O_3 by means of theoretical and experimental vibration spectra, *J. Phys. Chem. B*, 2006, **110**, 8320–8324.
43 Y. Cai, B. Zhang, H. Yu, X. Ji, J. Sun, X. Wang, Q. Qian, L. Li, A. Liu, W. Tan, F. Gao and L. Dong, Shielding ceria based catalysts from SO_2 poisoning in NH_3-SCR reaction: Modification effect of acid metal oxides, *Appl. Catal., B*, 2024, **342**, 123424.
44 R. Chen, X. Fang, J. Li, Y. Zhang and Z. Liu, Mechanistic investigation of the enhanced SO_2 resistance of Co-modified MnO_x catalyst for the selective catalytic reduction of NO_x by NH_3, *Chem. Eng. J.*, 2023, **452**, 139207.
45 Z. Zhang, R. Li, M. Wang, Y. Li, Y. Tong, P. Yang and Y. Zhu, Two steps synthesis of $CeTiO_x$ oxides nanotube catalyst: Enhanced activity, resistance of SO_2 and H_2O for low temperature NH_3-SCR of NO_x, *Appl. Catal., B*, 2021, **282**, 119542.
46 R. Chen, X. Fang, J. Li, Y. Zhang and Z. Liu, Mechanistic investigation of the enhanced SO_2 resistance of Co-modified MnO_x catalyst for the selective catalytic reduction of NO_x by NH_3, *Chem. Eng. J.*, 2023, **452**, 139207.
47 B. Liang, J. Ma, X. Su, C. Yang, H. Duan, H. Zhou, S. Deng, L. Li and Y. Huang, Investigation on deactivation of Cu/ZnO/Al_2O_3 catalyst for CO_2 hydrogenation to methanol, *Ind. Eng. Chem. Res.*, 2019, **58**, 9030–9037.
48 M. Sahibzada, D. Chadwick and I. S. Metcalfe, Hydrogenation of carbon dioxide to methanol over palladium-promoted Cu/ZnO/Al_2O_3 catalysts, *Catal. Today*, 1996, **29**, 367–372.
49 T. W. Hansen, A. T. Delariva, S. R. Challa and A. K. Datye, Sintering of catalytic nanoparticles: Particle migration or ostwald ripening?, *Acc. Chem. Res.*, 2013, **46**, 1720–1730.
50 M. Salavati-Niasari and F. Davar, Synthesis of copper and copper(I) oxide nanoparticles by thermal decomposition of a new precursor, *Mater. Lett.*, 2009, **63**, 441–443.
51 Y. Zhang, Y. Yang, H. Han, M. Yang, L. Wang, Y. Zhang, Z. Jiang and C. Li, Ultra-deep desulfurization via reactive adsorption on Ni/ZnO: The effect of ZnO particle size on the adsorption performance, *Appl. Catal., B*, 2012, **119–120**, 13–19.
52 J. Wu, M. Saito, M. Takeuchi and T. Watanabe, The stability of Cu/ZnO-based catalysts in methanol synthesis from a CO_2-rich feed and from a CO-rich feed, *Appl. Catal., A*, 2001, **218**, 235–240.
53 M. Mousavi-Kamazani, Z. Zarghami and M. Salavati-Niasari, Facile and novel chemical synthesis, characterization, and formation mechanism of copper sulfide (Cu_2S, Cu_2S/CuS, CuS) nanostructures for increasing the efficiency of solar cells, *J. Phys. Chem. C*, 2016, **120**, 2096–2108.
54 R. K. Sithole, L. F. E. Machogo, M. J. Moloto, S. S. Gqoba, K. P. Mubiayi, J. Van Wyk and N. Moloto, One-step synthesis of Cu_3N, Cu_2S and Cu_9S_5 and photocatalytic degradation of methyl orange and methylene blue, *J. Photochem. Photobiol., A*, 2020, **397**, 112577.
55 M. Sookhakian, Y. M. Amin, W. J. Basirun, M. T. Tajabadi and N. Kamarulzaman, Synthesis, structural, and optical properties of type-II ZnO–ZnS core–shell nanostructure, *J. Lumin.*, 2014, **145**, 244–252.
56 C. Ramamoorthy and V. Rajendran, Synthesis and characterization of CuS nanostructures: Structural, optical, electrochemical and photocatalytic activity by the hydro/solvothermal process, *Int. J. Hydrogen Energy*, 2017, **42**, 26454–26463.
57 R. Ma, J. Stegemeier, C. Levard, J. G. Dale, C. W. Noack, T. Yang, G. E. Brown and G. V. Lowry, Sulfidation of copper

oxide nanoparticles and properties of resulting copper sulfide, *Environ. Sci.:Nano*, 2014, **1**, 347–357.

58 Y.-C. Li, S.-N. Zhuo, B. Peng, X.-B. Min, H. Liu and Y. Ke, Comprehensive recycling of zinc and iron from smelting waste containing zinc ferrite by oriented transformation with SO_2, *J. Cleaner Prod.*, 2020, **263**, 121468.

59 H. Chen, C. Dai, F. Xiao, Q. Yang, S. Cai, M. Xu, H. J. Fan and S. Bao, Reunderstanding the reaction mechanism of aqueous Zn–Mn batteries with sulfate electrolytes: Role of the zinc sulfate hydroxide, *Adv. Mater.*, 2022, **34**, 2109092.

60 L. Zhang, D. Wang, Y. Liu, K. Kamasamudram, J. H. Li and W. Epling, SO_2 poisoning impact on the NH_3-SCR reaction over a commercial Cu-SAPO-34 SCR catalyst, *Appl. Catal., B*, 2014, **156–157**, 371–377.

61 J. D. Bjerregaard, M. Votsmeier and H. Grönbeck, Mechanism for SO_2 poisoning of Cu-CHA during low temperature NH_3-SCR, *J. Catal.*, 2023, **417**, 497–506.

62 Y. Jangjou, D. Wang, A. Kumar, J. H. Li and W. S. Epling, SO_2 poisoning of the NH_3-SCR reaction over Cu-SAPO-34: Effect of ammonium sulfate versus other S-containing species, *ACS Catal.*, 2016, **6**, 6612–6622.

63 W. K. Su, Z. G. Li, Y. N. Zhang, C. C. Meng and J. H. Li, Identification of sulfate species and their influence on SCR performance of Cu/CHA catalyst, *Catal. Sci. Technol.*, 2017, **7**, 1523–1528.

64 M. Happel, Y. Lykhach, N. Tsud, T. Skála, V. Johánek, K. C. Prince, V. Matolín and J. Libuda, SO_2 decomposition on Pt/CeO_2(111) model catalysts: On the reaction mechanism and the influence of H_2 and CO, *J. Phys. Chem. C*, 2012, **116**, 10959–10967.

65 M. S. Wilburn and W. S. Epling, Formation and decomposition of sulfite and sulfate species on Pt/Pd catalysts: An SO_2 oxidation and sulfur exposure study, *ACS Catal.*, 2019, **9**, 640–648.